

MLINE-VINS: Robust Monocular Visual-Inertial SLAM With Flow Manhattan and Line Features

Chao Ye, Haoyuan Li, Weiyang Lin, Xianqiang Yang

Abstract—In this paper we introduce MLINE-VINS, a novel monocular visual-inertial odometry (VIO) system that leverages line features and Manhattan Word assumption. Specifically, for line matching process, we propose a novel geometric line optical flow algorithm that efficiently tracks line features with varying lengths, which is do not require detections and descriptors in every frame. To address the instability of Manhattan estimation from line features, we propose a tracking-by-detection module that consistently tracks and optimizes Manhattan frame in consecutive images. By aligning the Manhattan World with the VIO world frame, the tracking could restart using the latest pose from back-end, simplifying the coordinate transformations within the system. Furthermore, we implement a mechanism to validate Manhattan frames and a novel global structural constraints back-end optimization. Extensive experiments results on various datasets, including benchmark and self-collected datasets, show that the proposed approach outperforms existing methods in terms of accuracy and long-range robustness. The source code of our method is available at: <https://github.com/LiHaoyuan/MLINE-VINS>.

Index Terms—Manhattan world, visual-inertial odometry (VIO), line optical flow, visual simultaneous localization and mapping (SLAM).

I. INTRODUCTION

ACCURACY of pose estimation is a critical factor in various fields, such as autonomous driving, augmented reality, and robotics. Simultaneous localization and mapping (SLAM) has proven to be an effective approach to address this challenge [1], [2]. Among SLAM techniques, visual-inertial odometry (VIO) is particularly popular due to its cost-effectiveness, accuracy, and robustness.

In VIO, point feature is widely used for camera pose estimation due to its simplicity and efficiency. Representative point-based VIO systems include MSCKF-VIO [3], OK-VINS [4] and VINS-MONO [5], with VINS-MONO being one of the most widely adopted algorithm. However, the performance of point-based VIO is affected by the number and spatial distribution of points and it significantly hindered in textureless environments, where the lack of texture leads to point loss. To address these limitations, line features are increasingly considered as a valuable complement to point features improving the robustness of VIO systems.

Line features are commonly found in low-texture environments, particularly in man-made environments [6]. To enhance the robustness of VIO systems, researchers have incorporated line features into VIO systems, such as PL-VINS [7], PL-VIO [8], UL-SLAM [9]. They demonstrate better performance

compared to point-only systems in textureless environments. However, a significant challenge in existing line-based VIO systems lies in the efficiency of line-matching, which is often time-consuming and unsuitable for real-time applications. Traditional methods rely on LSD [10] to extract line features and LBD [11] to match line features in every frame, both of which are computationally expensive and impractical for real-time use. Wang et al. [12] proposed a deep learning-based line flow algorithm, but it still requires to detect lines in every frame. Xu et al. [13] introduced a geometric-based line tracking algorithm that achieves real-time performance. Compared to deep-learning based method, the method is more efficient do not require obtain detections and descriptors. However, it does not account for changes in line segment lengths in across frames. These limitations restrict the effectiveness of current line optical flow algorithms. To address these issues, we propose a novel line optical flow algorithm capable of tracking line features with varying lengths in consecutive frames.

Although line features enhance VIO performance in textureless environments, they fail to address the drift problem during long-term operation. The Manhattan world (*MW*) assumption [14], a structural regularity in artificial environments, provides additional long-term information. In such environments, planes or lines align with three perpendicular predominant directions. This characteristic has been widely used to decouple rotation and translation in visual systems [15]. However, few studies have leveraged *MW* information to optimize VIO systems. Some researchers [16] indirectly incorporate *MW* constraints covertly by aligning line features with the *MW*'s axes, significant reductions in cumulative error. Typically, the *MW* is established using three orthogonal vanishing points in camera frame [17], which are formed by the intersections of parallel lines in the image. Researchers have explicitly utilized vanishing points to construct constraints for system optimization [18]. However, extracting vanishing points is computationally expensive and the global constraints between the *MW* and line features are often overlooked. In this paper, we propose a fast and robust tracking-by-detection module to track Manhattan in consecutive frames. For *MW* validation, we introduce a pose-guided Manhattan verification method. Additionally, we propose a novel back-end optimization framework that incorporates both local and global Manhattan constraints.

To address these issues, we propose a novel VIO system called MLINE-VINS integrates line features and the *MW* assumption to enhance the robustness and accuracy of the system. The primary contributions of this paper are as follows:

- We propose a novel optical flow algorithm based on geometric to efficiently and reliably track line features

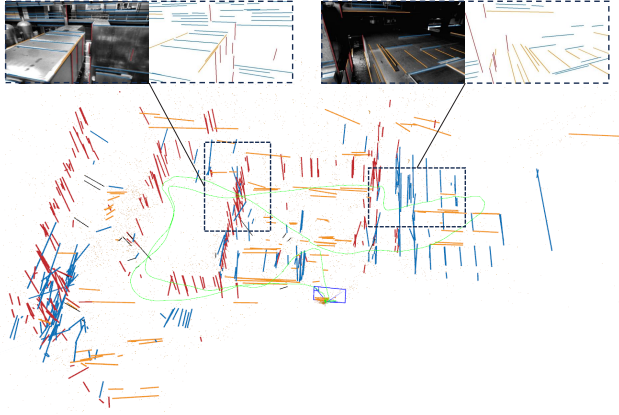


Fig. 1. Results of the proposed VIO system on EuRoC *MH05*. The blue, yellow, and red lines represent 3D structural lines along the X, Y, and Z directions, respectively. The green trajectory indicates the camera’s historical poses. The black points represent 3D points, and the 2D structural lines extracted from the RGB image are also shown at the top.

with changes in length across consecutive frames, outperforming traditional methods.

- We propose an efficient tracking-by-detection module for tracking Manhattan in consecutive frames. Initially, tracked lines are used to estimate the initial Manhattan, which is then refined with both tracked and supplementary lines. Additionally, a pose-guided Manhattan verification method is introduced for validation in the back-end.
- We estimate a novel global constraints back-end optimization framework that leverages structural information among all frames.
- Extensive experiments on benchmark and collected datasets demonstrate that the proposed VIO system outperforms existing point-line monocular VIO systems.

II. RELATED WORK

In this work, we focus on pose estimation in structural environments using monocular visual-inertial odometry. Accordingly, we categorize related studies into two areas: line based SLAM and SLAM aided by structural regularity .

A. Line Based SLAM

Compared to points, line features are good components to enhance VIO performance in low-texture environments. Therefore, many studies, such as PL-VIO [8], PL-VINS [7] have incorporated line features as landmarks in SLAM systems. However, the efficiency of line matching remains a significant challenge for real-time applications in line-based SLAM systems. Traditional methods rely on geometric relationships [19] between frames to identify candidate lines and use RANSAC [20] for selection. These methods, however, require accurate prior pose information, which conflicts with the objectives of SLAM systems. Alternatively, widely used descriptor-based matching methods like LBD [11] and MSLD [21] do not require prior information. However, extracting descriptors is computationally expensive due to repetitive processing and cannot handle changes in line lengths.

Some researchers have applied the optical flow concept, originally used for point features, to design line flow algorithms [22], often overlooking the geometric constraints of line features. In [23] and [12], the authors propose a method using line optical flow to guide line extraction from LSD in the next frame, which is time-consuming. EPLF-VINS [13] introduces a line flow tracking method based on the grayscale invariance hypothesis [24] and line geometric constraints, but it does not account for changes in the lengths of line segments.

B. SLAM Aided by Structural Regularity

The structural regularity of *MW* is widely used to enhance SLAM system performance. In VIO, *MW* is typically indirectly used to optimize the representation of line features, but it is not incorporated into the back-end optimization. Struct VIO [16] covertly incorporates *MW* constraints by aligning line features with the directions of the *MW*’s axes, achieving excellent performance.. But the *MW* constraints are only used in the front-end and are not utilized in the back-end optimization. UV-SLAM [18] introduces additional constraints between vanish points and linefeatures into the optimization problem. This improves the performance of the VIO system. However, these *MW* constraints are only applied within local optimization, neglecting the global constraints between *MW* and line features.

Manhattan frames are typically estimated by clustering planar normal vectors. For purely visual scenarios, researchers use vanishing points to indirectly get Manhattan. The 2-line method [17] clusters intersections of lines projected onto a sphere and selects the most reliable Manhattan. While a Manhattan searching method [25] is also proposed to find Manhattan on a image. However, these methods rely heavily on the number and distribution of line features, making them less robust in complex indoor environments. Since these approaches estimate Manhattan from individual images, they fail to address the challenge of matching coordinate axes in consecutive frames. Additionally, most Manhattan-based SLAM systems commonly use LSD for line extraction and the 2-line method for Manhattan estimation, which are both time-consuming and lack robustness.

In this paper, we take a step further to propose a novel VIO system by addressing the aforementioned issues. Our line optical flow algorithm efficiently tracks line features across consecutive frames, accommodating changes in length. Additionally, a novel tracking-by-detection module can continuous track Manhattan, which is fast and robust in complex indoor environments. And a pose guided Manhattan frame verification is proposed to validate the Manhattan. Finally, we leverage the *MW* model to incorporate both global and local constraints in the back-end optimization.

III. SYSTEM OVERVIEW

This paper introduces MLINE-VINS, a novel monocular visual-inertial odometry system designed for robust performance in complex indoor environments. The pipeline of our system is shown in Fig. 2. We propose innovative strategies for Manhattan and line feature tracking, coupled with back-end

optimization leveraging Manhattan constraints. Our approach focuses on improving robustness and accuracy of the VIO system in challenging indoor environments.

A. Notation and Manhattan Model

In this paper, we use the IMU frame as the body frame, and the notations are defined in Table I. $\mathbf{R} \in SO(3)$, $\mathbf{t} \in \mathbb{R}^3$ represent the rotation matrix and translation vector, respectively, and $\mathbf{T} = \begin{bmatrix} \mathbf{R} & \mathbf{t} \\ 0 & 1 \end{bmatrix}$ denotes the transformation matrix.

TABLE I
SOME IMPORTANT NOTATIONS

| Notations | Explanation |
|-------------|---|
| \times | Cross product operation |
| $(\cdot)^w$ | A vector (\cdot) in global world frame |
| $(\cdot)^c$ | vector (\cdot) in camera frame |
| $(\cdot)^b$ | vector (\cdot) in IMU frame |
| $(\cdot)^M$ | vector (\cdot) in Manhattan frame |
| T_b^c | The extrinsic matrix from IMU frame to camera frame |

The *MW* is a static box world with three orthogonal directions, known as the principal axes. Most line features in the scene are aligned with one of these principal axes. We define Manhattan frame observation in the camera frame as the Manhattan Frame (*MF*) which can be expressed as $\mathbf{R}_M^{c_i}$. As shown in Fig. 3, the relative rotation between two *MFs*, $\mathbf{R}_{c_i}^{c_j}$ can be easily computed as follows:

$$\mathbf{R}_{c_i}^{c_j} = \mathbf{R}_M^{c_j} (\mathbf{R}_M^{c_i})^{-1} \quad (1)$$

We apply the *MW* assumption to enhance the system's robustness in complex indoor environments.

B. Local Visual-Inertial Odometry

The local VIO system consists of three components: measurement processing, system initialization, and nonlinear optimization.

1) *Measurement Processing*: The system receives RGB images and IMU messages as inputs. For images, point and line features are processed in parallel. When the first image is input, point and line features are extracted using Shi-Tomasi [26] and modified EDLines algorithm. If line features are available, the system detects *MFs* and classifies lines into three principal directions using the 2-line method [17]. In consecutive frames, point features are matched using the KLT tracker [27], line features are matched with an improved line optical flow method for, and *MFs* are matched using a proposed tracking-by-detection module. If *MW* tracking fails, the last camera pose state in the back-end is used as the initial value to restart tracking. For IMU messages, preintegration is accumulated between keyframes, following the same approach as VINS-MONO [5].

2) *System Initialization*: After collecting sufficient information from the front-end, the system initializes the primary state, which include scaling parameter s , pose \mathbf{T}_{b_i} , gravity \mathbf{g} , velocity \mathbf{v}_i , line 3D representation \mathbf{o}_i and IMU gyroscope bias $\delta \mathbf{b}_w$.

The transformation $\mathbf{T}_{c_i}^{c_0}$ is initialized using the Structure from Motion (*SFM*) method, leveraging visual features in a sliding window. It is then converted to $\mathbf{T}_{b_i}^{c_0}$ using the extrinsic matrix \mathbf{T}_b^c . By simultaneously considering *SFM* results and IMU preintegration, the gyroscope bias $\delta \mathbf{b}_w$ is estimated through rotation differences. The gravity \mathbf{g} , velocity \mathbf{v}_i , and scale s are determined by minimizing location and velocity residuals. To simplify the relationship between *MW* and real VIO world frame, the VIO world frame is aligned with the *MW*. Consequently, the $\mathbf{T}_{b_i}^{c_0}$ is transformed into $\mathbf{T}_{b_i}^M$.

For line features, a 3D line $\mathcal{L} = [\mathbf{n}^T, \mathbf{d}^T]^T$ is parameterized using Plücker representation. This representation comprises the line direction \mathbf{d} and normal vector \mathbf{n} of the plane formed by the line and camera center. It is initialized using Plücker matrix L^* , which is derived from the intersection of two planes π_1, π_2 as shown below:

$$\mathbf{L}^* = \begin{bmatrix} [\mathbf{d}]_{\times} & \mathbf{n} \\ -\mathbf{n}^T & 0 \end{bmatrix} = \pi_1 \pi_2^T - \pi_2 \pi_1^T \quad (2)$$

3) *Nonlinear Optimization*: Following the system initialization, the state is optimized within a sliding-window.

Line Orthogonal Representation: The Plücker representation facilitates spatial transformations of lines but is impractical for optimization due to over-parameterization. Therefore, a more concise representation is adopted for optimizing line features. The orthogonal representation is defined as:

$$\mathbf{o}_i = [\psi_i, \phi_i] \quad (3)$$

where $\psi_i = \left[\frac{\mathbf{n}}{\|\mathbf{n}\|}, \frac{\mathbf{d}}{\|\mathbf{d}\|}, \frac{\mathbf{n} \times \mathbf{d}}{\|\mathbf{n} \times \mathbf{d}\|} \right]$, and ϕ_i is the distance between the line and the camera center.

Optimization State The full state vector χ is defined as follows:

$$\begin{aligned} \chi &= [\mathbf{x}_0, \mathbf{x}_1, \dots, \mathbf{x}_n, \lambda_0, \lambda_1, \dots, \lambda_m, \mathbf{o}_0, \mathbf{o}_1, \dots, \mathbf{o}_k] \\ \mathbf{x}_i &= [\mathbf{q}_{b_i}^M, \mathbf{t}_{b_i}^M, \mathbf{v}_i^M, \mathbf{b}_a, \mathbf{b}_w] \\ \mathbf{o}_i &= [\psi_i, \phi_i] \end{aligned} \quad (4)$$

$\mathbf{q}_{b_i}^M$ is the quaternion form of $R_{b_i}^M$. Note that all states are estimated in the *MW* frame.

The optimization problem is formulated as a visual-inertial adjustment and can be expressed as below:

$$\begin{aligned} & \min_{\chi} \{ \|r_p - \mathbf{H}_p \chi\|^2 + \sum_{i \in \mathcal{B}} \|r_{\mathcal{B}}(z_{i+1}^i, \chi)\|_{Cov_{b_{i+1}}^{b_i}}^2 \\ & + \sum_{(i,j) \in \mathcal{P}} \rho_p \|r_{\mathcal{P}}(z_{P_j}^{c_i}, \chi)\|_{Cov_{P_j}^{c_i}}^2 + \sum_{(i,k) \in \mathcal{L}} \rho_l \|r_{\mathcal{L}}(z_{L_k}^{c_i}, \chi)\|_{Cov_{L_k}^{c_i}}^2 \\ & + \sum_{(i,m) \in \mathcal{M}} \|r_{\mathcal{M}}(z_{M_m}^{c_i}, \chi)\|_{Cov_{M_m}^{c_i}}^2 \\ & + \sum_{(i,n) \in \mathcal{L}_{struct}} \|r_{\mathcal{L}_{struct}}(z_{L_m}^{c_i}, \chi)\|_{Cov_{L_m^{struct}}^{c_i}}^2 \} \end{aligned} \quad (5)$$

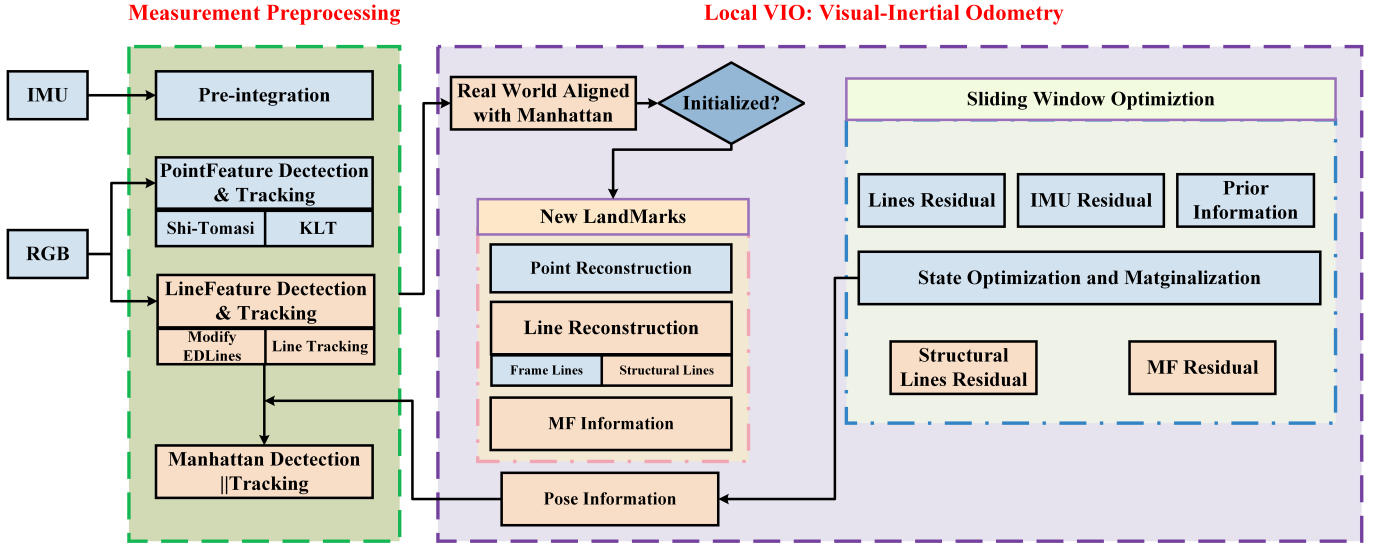


Fig. 2. Overview of MLINE-VINS. The orange boxes highlight the new components introduced in this paper. Upon receiving the RGB input, points and lines are extracted and tracked in parallel. The Manhattan tracking-by-detection module is then executed to estimate MFs in consecutive images, with each line being clustered according to a principal axis. If the MF is lost, the last camera state from the back-end is used as the initial value to restart tracking. After system initialization, the VIO world frame is aligned with the MW , and optimization is performed using the local and global constraints of Manhattan and structural lines.

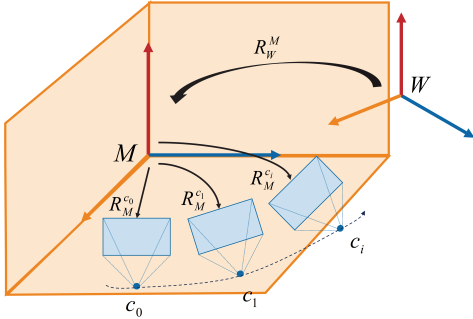


Fig. 3. Rotation estimation between camera frame and MW . The extrinsic matrix R_W^M represents the rotation between VIO world frame and MW . The rotation changes between MFs in camera coordinate are represented by $R_M^{c_i}$.

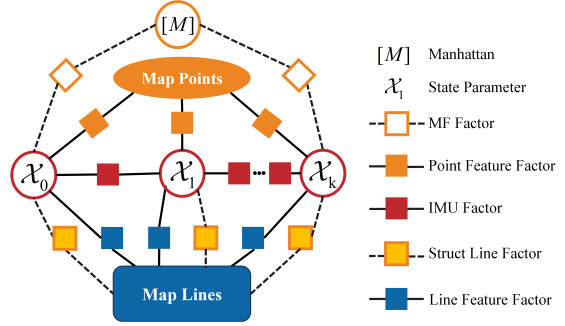


Fig. 4. Factor graph for MLINE-VINS. The 'Map points' and 'Map lines' nodes represent all point and line features within the sliding window. 'Map Lines' include both structural and non-structural lines. Structural lines provide both reprojection and structural constraints, while non-structural lines only contribute reprojection constraints.

the Huber norm ρ_p [28] is defined as:

$$\rho_p(x) = \begin{cases} x & x \leq 1 \\ 2\sqrt{x} - 1 & x > 1 \end{cases} \quad (6)$$

where $r_B, r_P, r_L, r_M, r_{\mathcal{L}_{struct}}$ are residuals for IMU, point, line, Manhattan and structural line features respectively. \mathcal{P}, \mathcal{L} are 3D points and lines triangularized in the sliding window, while \mathcal{M} denotes the MF observation and \mathcal{L}_{struct} refers to the structural lines among the set of lines \mathcal{L} . The covariance matrix of the measurement is denoted as Cov , and z represents the measurement. The prior message from the marginalization of old states is represented as $[r_p, \mathbf{H}_p]$. The factor graph for the defined cost function is shown in Fig. 4. If there are no MFs or structural lines, only point and line residuals are used for optimization. The Ceres Solver [29] is employed to solve the nonlinear optimization problem.

IV. IMPLEMENTATION OF KEY COMPONENTS

A. Novel Line Optical Flow Algorithm

Previous methods for line features detection and matching are often time consuming and inefficient. Common approaches, such as using LSD for line detection and LBD for descriptor-based matching, are time-consuming and affected by repetitive textures. To address these issues, this paper introduces a novel line optical flow algorithm. The algorithm operates in two stages: 1) Line Feature Initialization; 2) Line Optical Flow Tracking. By eliminating the need to detect and match lines in every frame, the proposed approach is highly suitable for real-time applications.

1) *Line Feature Initialization*: In the first frame, a modified EDLines (MED) is used to extract line features. For robust feature tracking, line features are uniformly distributed across the image and co-linear features are merged. If the number of

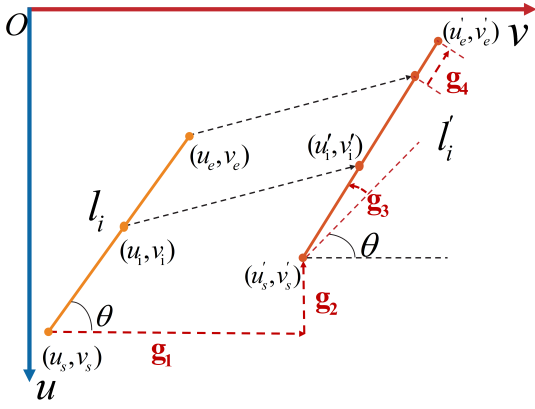


Fig. 5. Diagram of Line feature tracking model. l_i represents a line feature in frame F_t , and l'_i is the tracked line feature in frame $F_{t+\delta t}$. g_1, g_2, g_3, g_4 denote the changes in the horizontal coordinate, vertical coordinate, angle and length changes of the line feature, respectively.

line features is below the set threshold, the grayscale threshold parameter of MED is reduced, and line extraction is repeated..

2) *Line Optical Flow Tracking*: The primary concept is based on the grayscale invariance assumption. At time $t + \delta t$, a pixel (u, v) at time t moves to (u', v') , while maintaining a constant grayscale value, expressed as:

$$I(u, v, t) = I(u + \delta u, v + \delta v, t + \delta t) \quad (7)$$

Using the Taylor expansion on the right-hand of Eq. (7), we obtain:

$$I(u, v, t) = I(u, v, t) + \frac{\partial I}{\partial u} \delta u + \frac{\partial I}{\partial v} \delta v + \frac{\partial I}{\partial t} \delta t \quad (8)$$

simplify the above equation, we obtain:

$$\mathbf{I}_t = - \begin{bmatrix} I_u & I_v \end{bmatrix} \begin{bmatrix} \frac{du}{dt} \\ \frac{dv}{dt} \end{bmatrix} \quad (9)$$

where \mathbf{I}_t represents the gray temporal change in image, I_u and I_v denote the spatial intensity gradients at the point. Every pixel in frame F_t adheres to this relationship. An additional constraint for line features is introduced below.

A line feature l_i at time t is defined as:

$$\mathbf{l}_i = [(u_s, v_s), (u_1, v_1), \dots, (u_i, v_i), (u_e, v_e)] \quad (10)$$

where (u_s, v_s) is start point, and (u_e, v_e) is endpoint.

As shown in Fig. 5, during δt , l_i moves to l'_i on the image. The relationship between the same line in two consecutive frames is expressed as follows:

$$\begin{aligned} u'_i &= u_i + g_1 + (l_i + g_4 l_i) \cos(\alpha + g_3) - l_n \cos \alpha \\ v'_i &= v_i + g_2 + (l_i + g_4 l_i) \sin(\alpha + g_3) - l_n \sin \alpha \end{aligned} \quad (11)$$

where g_1 and g_2 represent the position change of the starting point, g_3 denotes the angle change, and g_4 indicates the change in line length.

By simplifying the equation and neglecting second-order small quantities, the equation can be rewritten as follows:

$$\begin{aligned} u'_i &= u_i + g_1 + g_3(v_i - v_s) + g_4(u_i - u_s) \\ v'_i &= v_i + g_2 - g_3(u_i - u_s) + g_4(v_i - v_s) \end{aligned} \quad (12)$$

From Eq. (12), we can derive:

$$\begin{aligned} \frac{du_i}{dt} &= \frac{dg_1}{dt} - \frac{dg_3}{dt}(v_i - v_s) + \frac{dg_4}{dt}(u_i - u_s) \\ \frac{dv_i}{dt} &= \frac{dg_2}{dt} - \frac{dg_3}{dt}(u_i - u_s) + \frac{dg_4}{dt}(v_i - v_s) \end{aligned} \quad (13)$$

Then we define $\frac{dg_1}{dt}$, $\frac{dg_2}{dt}$, $\frac{dg_3}{dt}$ and $\frac{dg_4}{dt}$, as $\delta g_1, \delta g_2, \delta g_3$ and δg_4 , respectively. Consequently, Eq.(13) can be rewritten as:

$$\begin{bmatrix} u & v \end{bmatrix} = \begin{bmatrix} 1 & 0 & -(v_i - v_s) & u_i - u_s \\ 0 & 1 & (u_i - u_s) & v_i - v_s \end{bmatrix} \begin{bmatrix} \delta g_1 \\ \delta g_2 \\ \delta g_3 \\ \delta g_4 \end{bmatrix} \quad (14)$$

Each point on the line l_i satisfies Eq.(14), forming an overdetermined linear equation with $\delta g_1, \delta g_2, \delta g_3$ and δg_4 . This problem can be solved by using the Gauss-Newton method. To enhance feature tracking accuracy, the algorithm is integrated into a pyramid multi-scale optical flow framework. Longer lines are considered more reliable for feature tracking, so co-linear short lines are merged. Based on the gradient, the starting and endpoints of the lines are extended or merged. If the number of tracked lines is insufficient, MED is executed to extract additional features.

B. Tracking-By-Detection Algorithm for Manhattan

The runtime and accuracy of MFs detection significantly influence the system's overall performance. The number and distribution of structural lines primarily influence the effectiveness of Manhattan detection. To address this, we propose an algorithm that incorporates line-tracking results to track MFs in consecutive frames. This method is designed to improve the system's robustness in complex indoor environments.

1) *Initialization*: The detection module involves two essential steps: Detecting MF during the initial stage, and selecting the most reliable one. The 2-lines [17] method is employed to identify all potential MFs in a given frame, and then the most reliable one is selected. Since the result depends on the number and distribution of line features, validity is verified using the z-axis of the MF and vertical lines. If all conditions are satisfied,, the $MF R_M^{c_i}$ is initialized.

2) *Tracking*: Since the original 2-lines method is not robust in scenarios with insufficient line features, we propose a tracking-by-detection module to track MF in consecutive frames. As illustrated in Fig. 6, this module utilizes prior structural lines information from the previous frame to estimate MF in the current frame. The three principal axis directions of the MF can be interpreted as the spatial positions of vanishing points.

$$\mathbf{R}_M^{c_i} = [vp_1^{c_i} \quad vp_2^{c_i} \quad vp_3^{c_i}] \quad (15)$$

An illustration of the proposed algorithm is presented in Fig. 6. This module classifies tracking scenarios into three categories based on the number of structural lines.

Structural lines tracked in three directions: If the number of lines tracked in three principal directions is n_1, n_2 and n_3 ($n_i > 2, i = 1, 2, 3$), the MF in the current frame can directly estimate an initial value through the intersection of any two lines on a unit sphere. The initial value is defined as

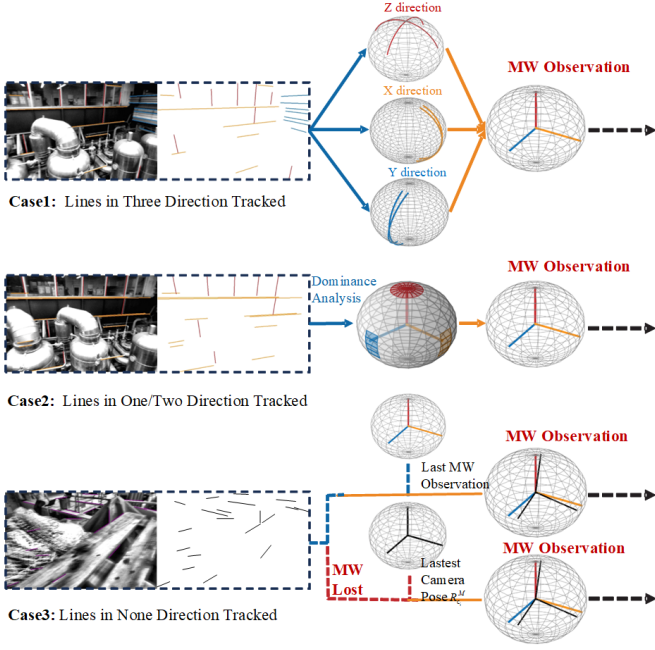


Fig. 6. Illustration of Manhattan Tracking module. Case 1: Structural lines tracked in three directions. MF is estimated by three vanishing points, formed by the intersection of lines in three directions on a normal sphere. Case 2: Structural lines tracked in one or two directions. MF is estimated by the polar grid with weights related to length of lines. Case 3: Structural lines tracked failure. If the Manhattan exists in the previous frame, optimize it with current lines; Otherwise, optimize MF using the last camera position from back-end with lines.

$R_M^{c_i'} = [vp_1', vp_2', vp_3']$. Subsequently, structural line features are used to optimize this value.

The start and end points of a line l_i in the image are defined as $[u_{i_s}, v_{i_s}]$ and $[u_{i_e}, v_{i_e}]$, respectively. The representation of a 3D line can be obtained using the equation below:

$$\begin{aligned} p_{i_s}^{c_i} &= [u_{i_s} \quad v_{i_s} \quad 1] \\ p_{i_e}^{c_i} &= [u_{i_e} \quad v_{i_e} \quad 1] \\ l_i^{c_i} &= p_{i_s}^{c_i} \times p_{i_e}^{c_i} \end{aligned} \quad (16)$$

The relationship between l_i and its corresponding vanishing point direction is parallel. Therefore, $R_M^{c_i'}$ can be optimized using:

$$error = \sum_{i=1}^{n_1} l_i^{c_i} * vp_1 + \sum_{i=1}^{n_2} l_i^{c_i} * vp_2 + \sum_{i=1}^{n_3} l_i^{c_i} * vp_3 \quad (17)$$

Structural lines tracked in one or two directions: If lines are traced in only one or two directions, the scoring strategy for potential vanishing points is modified. In 2-lines method, intersections of every two lines are mapped to a polar grid \mathcal{G} with weights proportional to length. And the best MF is chosen based on the highest score. Structural lines are more reliable than common lines for identifying the MF s. For a point p on an unit sphere, its latitude ϕ_1 and longitude ϕ_2 can be calculated, where $\phi_1 \in [0, \pi/2]$ and $\phi_2 \in [0, 2\pi]$. The polar grid $\mathcal{G}(i, j)$ is initialized with a size of 90×360 , and the corresponding grid $\mathcal{G}(i, j)$ is updated using the following equation:

$$\mathcal{G}(i, j) = \mathcal{G}(i, j) + \|\lambda_1\| * \|\lambda_2\| * \sin(2\theta) \quad (18)$$

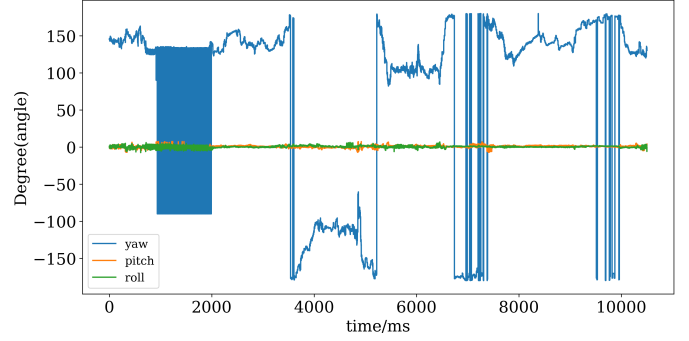


Fig. 7. The angle error between VIO world frame and MW .

where λ is an adjustable weight, if the lines l_1, l_2 are structural lines, $\lambda = 10$; otherwise, $\lambda = 1$.

Structural lines tracked failure When no structural lines are successfully tracked, the MF from the previous frame is used as the initial value to categorize lines in n_1, n_2 and n_3 . This approach is based on the assumption that the MF changes minimally between two adjacent frames. If the MF is unavailable in the previous frame, the latest camera pose from the back-end is used as the initial value. This is feasible because the MW is aligned with the VIO world frame, as explained in the next section. The MF is then optimized according to Eq.(17)

The updated vp_1, vp_2, vp_3 are used to compose $R_M^{c_i}$, ensuring that $R_M^{c_i}$ retains the properties of a valid rotation matrix. Since the 2-lines method is inherently random and disorder, the order and reliability of the MF need to be verified. By incorporating these approaches, the tracking-by-detection module achieves consistency and reliability even in complex indoor environments.

C. VIO World Frame Algin with Manhattan World

Since the MW and VIO world frames are not aligned in the same coordinate system, we investigate the relationship between them. In a sequence such as *MH01*, ten consecutive frames are used for initialization to get VIO world frame. To obtain the MW , the MF in the camera frame is transformed into the IMU frame. The angular error between the VIO world frame and MW is illustrated in Fig.7. Due to the yaw being unobservable during VINS-MONO initialization, its value is unstable. The differences in roll and pitch are minimal, indicating that the z-axis direction of the MW and VIO world frame are parallel. Furthermore, there is an implicit characteristic in indoor environment where building plumb lines are parallel to the direction of gravity. Consequently, the z-axis of the MW corresponds to the direction of gravity. After VIO initialization, the body frame is expressed in the world frame as $R_{b_i}^W$. In the camera frame, the MW is expressed as $R_{c_i}^M$. The relationship between these two coordinate systems is given as follows:

$$\mathbf{R}_W^M = \mathbf{R}_{c_i}^M \mathbf{R}_b^c (\mathbf{R}_{b_i}^W)^{-1} \quad (19)$$

Thus, the poses can be transformed from the VIO world frame to the MW using the following relationship:

$$\mathbf{R}_{b_i}^M = \mathbf{R}_W^M \mathbf{R}_{b_i}^W \quad (20)$$

After the VIO world frame is aligned with the MW , it becomes easier to utilize the characteristics of the MW and restart tracking using the state from the back-end. Additionally, the yaw angle can also be observed through the MW .

D. Pose Guided Manhattan Frame Estimation Verification

However, the results of MF estimation are not always reliable, and incorrect results can negatively impact rotation estimation. To enhance system robustness, verification of the MFs is necessary. The pose error of VIO remains small over a short period within the sliding window. Considering two frames F_i and F_k in the VIO local window, the relative rotation between them should approximately equal the ground truth, $\mathbf{R}_{i,k}^{MF} \approx \mathbf{R}_{i,k}^{VIO}$. The reliability of the MFs is assessed using this relationship.

The local window consists of consecutive frames, i.e., F_{k-n}, \dots, F_{k+n} . The relative rotation between F_i and other frames in window, $\Delta \mathbf{R}_{i,k}^{MF}$ and $\Delta \mathbf{R}_{i,k}^{VIO}$ are computed using MFs and VIO, respectively.

Using Eq.(21), the average angular error can be calculated as follows:

$$error_{\mathbf{R}} = \frac{1}{2n} \sum_{i=k-n}^{k+n} \mathbf{Angle}(\Delta \mathbf{R}_{i,k}^{MF} (\Delta \mathbf{R}_{i,k}^{VIO})^{-1}) \quad (21)$$

where the function of \mathbf{Angle} is defined as follows:

$$\mathbf{Angle}_{\mathbf{R}} = \arccos(\min(1, \max(-1, \frac{\text{trace}(\mathbf{R}) - 1}{2}))) \quad (22)$$

If the $error_{\mathbf{R}}$ is below than the threshold $D_{\mathbf{Angle}}$ (e.g., $D_{\mathbf{Angle}} = 0.5$ in this paper), the MF is deemed reliable. Otherwise, it is considered unreliable and the MF will be discarded.

E. Line Measurement Model

For a 3D line \mathcal{L}_k , we first transform its Plücker representation from the Manhattan frame $(\cdot)^M$ to the camera frame $(\cdot)^{c_i}$ as follows:

$$L_k^{c_i} = \begin{bmatrix} \mathbf{n}_c \\ \mathbf{d}_c \end{bmatrix} = T_M^{c_i} * \mathcal{L}_k = \begin{bmatrix} \mathbf{R}_M^{c_i} & [t_M^{c_i}]_{\times} \mathbf{R}_M^{c_i} \\ 0 & \mathbf{R}_M^{c_i} \end{bmatrix} \begin{bmatrix} \mathbf{n}_w \\ \mathbf{d}_w \end{bmatrix} \quad (23)$$

Then, we use the following equation to project the line segment onto the image plane:

$$\mathbf{l}_k = \begin{bmatrix} l_1 \\ l_2 \\ l_3 \end{bmatrix} = \mathbf{K}_{proj} \mathbf{n}_k^{c_i} \quad (24)$$

where \mathbf{K}_{proj} represents the projection matrix and $\mathbf{n}_k^{c_i}$ denotes the direction of normalized line in $\{c_i\}$. As the image is in the normalized coordinate, \mathbf{K}_{proj} is an identity matrix.

As illustrated in Fig.8, the line residual is defined as the distance between the projected line and the observed line on the image plane. This relationship can be expressed as:

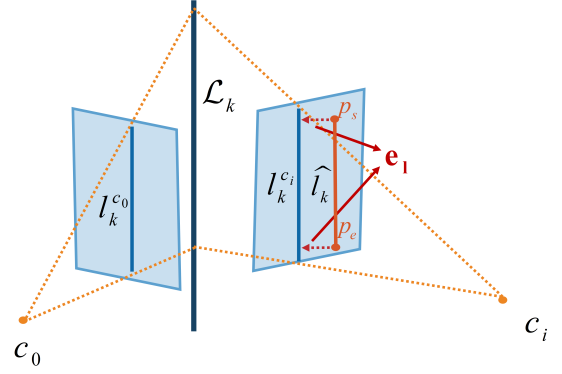


Fig. 8. Representation of line residual model. The blue line represents the reprojection of the 3D line in the image, while the orange line represents the observation. The residual e_l is calculated as the distance between the two lines.

$$e_l = \left[\begin{array}{c} d(\mathbf{l}_s, \mathbf{l}_k) \\ d(\mathbf{l}_e, \mathbf{l}_k) \end{array} \right] \quad (25)$$

where

$$d(\mathbf{l}_s, \mathbf{l}_k) = \frac{|\mathbf{l}_s^T \mathbf{l}_k|}{\|\mathbf{l}_k\|} \quad (26)$$

$\mathbf{l}_s = (u_s, v_s, 1)$ and $\mathbf{l}_e = (u_e, v_e, 1)$ represent the start and endpoint of observed line, respectively and let d denote the distance between point and re-projected line. The corresponding Jacobian J_l can be obtained using the chain rule:

$$J_l = \frac{\partial e_l}{\partial n_k^{c_i}} \frac{\partial n_k^{c_i}}{\partial L_k^{c_i}} \begin{bmatrix} \frac{\partial L_k^{c_i}}{\partial \delta x_i} & \frac{\partial L_k^{c_i}}{\partial \mathcal{L}_k} \frac{\partial \mathcal{L}_k}{\partial \delta o_i} \end{bmatrix} \quad (27)$$

with

$$\begin{aligned} \frac{\partial e_l}{\partial n_k^{c_i}} &= \begin{bmatrix} \frac{\partial e_l}{\partial n_k^{c_i}} & \frac{\partial e_l}{\partial n_k^{c_i}} & \frac{\partial e_l}{\partial n_k^{c_i}} \end{bmatrix} \\ &= \begin{bmatrix} -\frac{l_k(1)(l_s^T n_k^{c_i})}{\|l_k\|^3} + \frac{l_s(1)}{\|l_k\|} & -\frac{l_k(2)(l_s^T n_k^{c_i})}{\|l_k\|^3} + \frac{l_s(2)}{\|l_k\|} & \frac{1}{\|l_k\|} \\ -\frac{l_k(1)(l_e^T n_k^{c_i})}{\|l_k\|^3} + \frac{l_e(1)}{\|l_k\|} & -\frac{l_k(2)(l_e^T n_k^{c_i})}{\|l_k\|^3} + \frac{l_e(2)}{\|l_k\|} & \frac{1}{\|l_k\|} \end{bmatrix} \end{aligned} \quad (27)$$

F. Point Line Manhattan Union Back-end Optimization

In the back-end, we use MFs to constrain the rotation, and structural line features to establish local and global constraints.

1) *Manhattan Constraint on Rotation*: The VIO accumulates errors as the trajectory progresses. The MFs provides static information that can be used to correct the rotation drift. We define q_i^M and q_i^{VIO} as the quaternions of $R_{b_i}^M$ and $R_{b_i}^{VIO}$ in frame F_i . The residual of rotation is defined as follows:

$$e_i^M = 2(q_i^M \otimes (q_i^{VIO})^{-1})_{xyz} \quad (29)$$

And the Jacobian matrix J_M can be obtained as:

$$\begin{aligned} \frac{e_i^M}{\partial x_i} &= \begin{bmatrix} \frac{\partial e_i^M}{\partial q_i} & \frac{\partial e_i^M}{\partial t_i} \end{bmatrix} \\ &= \left[[q_i^M \otimes (q_i^{VIO})^{-1}]_{L_{xyz}} \quad 0 \right] \end{aligned} \quad (30)$$

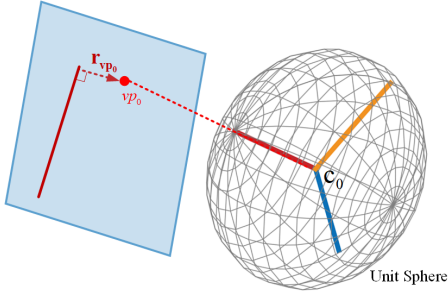


Fig. 9. Representation of Manhattan residual. The MF in the c_0 frame is shown on a unit sphere. The red point represents one of the vanishing points, and the red line on the image corresponds to a structural line. The distance between the vanishing point and the line represents the residual of the MF in that direction.

2) *Structural Lines Residual*: Structural lines provide more reliable information than common lines. Through the MF s, we can establish both local constraints using vanishing points in an image and global constraints using structural lines within MW . Suppose there are n triangulated line features in the sliding window, with n_1, n_2, n_3 lines in three respective directions. In frame F_i , the MF is expressed as $[vp_{1_i}, vp_{2_i}, vp_{3_i}]$. We can reproject all structural lines to the image plane, and they should conform to the structural regularity in frame F_i . The residual in F_i is given by Eq.(31)

$$e_i^{struct} = \sum_{i=1}^{n_1} d(vp_{1_i}, l) + \sum_{j=1}^{n_2} d(vp_{2_i}, l) + \sum_{k=1}^{n_3} d(vp_{3_i}, l) \quad (31)$$

Each frame in the sliding window can be estimated using the equation above. Meanwhile, global optimization can be performed by constraining all structural lines with the MW . The corresponding Jacobian J_{struct} with respect to the structural lines can be obtained as follows:

$$J_{struct} = \frac{\partial e_i^{struct}}{\partial n_k^{c_i}} \frac{\partial n_k^{c_i}}{\partial L_k^{c_i}} \begin{bmatrix} \frac{\partial L_k^{c_i}}{\partial \delta x_i} & \frac{\partial L_k^{c_i}}{\partial L_k} \frac{\partial L_k}{\partial \delta o_i} \end{bmatrix} \quad (32)$$

where

$$\frac{\partial e_i^{struct}}{\partial n_k^{c_i}} = \begin{bmatrix} \frac{\partial e_i^{struct}}{\partial n_k^{c_i}} & \frac{\partial e_i^{struct}}{\partial n_k^{c_i}} & \frac{\partial e_i^{struct}}{\partial n_k^{c_i}} \end{bmatrix}^T = \begin{bmatrix} -\frac{vp_i(1)(l_s^T n_k^{c_i})}{\|l_k\|^3} + \frac{vp_i(1)}{\|l_k\|} \\ -\frac{vp_i(2)(l_s^T n_k^{c_i})}{\|l_k\|^3} + \frac{vp_i(2)}{\|l_k\|} \\ \frac{1}{\|l_k\|} \end{bmatrix} \quad (33)$$

When there are no structural line features in the window, the back-end will automatically degenerate into a standard points-and-lines back-end.

V. EXPERIMENTAL RESULTS

In this section, we first evaluate our method on benchmark datasets. Then, real word self-recorded datasets are used to verify the system's effectiveness. We compare our method MLINE-VINS with advanced monocular methods, such as point-based method VINS-MONO [5], line-based method EPLF-VINS [13], PL-VINS [7], and structural constraints-based method Struct-VIO [16], UV-SLAM [18]. We use the

released versions and default parameters for all testing. All experiments are conducted on a PC with an Intel Core i7-7700 3.60GHz CPU and 24GB of RAM. For fair comparison, all systems are turned off loop closure and global bundle adjustment.

A. Benchmark Tests

1) *EuRoC Dataset Tests*: We first evaluate our method on the EuRoC dataset [30], a widely used benchmark for VIO. This dataset is collected by a micro aerial vehicle (MAV) equipped with stereo cameras and an IMU. Five sequences from the machine hall meet the assumptions of the MW . And the GT is provided by a laser tracker. For our evaluation, we utilize IMU data and images from the left-camera images to test our proposed method.

To evaluate the performance of each method, we use the root mean squared error (RMSE) as the evaluation metric. For each sequence, the average RMSE is calculated over 10 runs.

TABLE II
TRANSLATION RMSE ATE WITHOUT LOOP CLOSURE OF
EUROC DATASET(UNIT: M)

| Method | MH01 | MH02 | MH03 | MH04 | MH05 |
|-----------------|--------------|--------------|--------------|--------------|--------------|
| VINS-MONO [5] | 0.202 | 0.188 | 0.228 | 0.370 | 0.297 |
| Struct-VIO [16] | 0.079 | 0.145 | 0.103 | 0.130 | 0.182 |
| PL-VINS [7] | 0.216 | 0.193 | 0.218 | 0.247 | 0.325 |
| EPLF-VINS [13] | 0.140 | 0.088 | 0.114 | 0.182 | 0.182 |
| UV-SLAM [18] | 0.139 | 0.094 | 0.189 | 0.261 | 0.188 |
| MLINE-VINS | 0.074 | 0.072 | 0.093 | 0.196 | 0.130 |

Table II presents the absolute translation error (ATE) results of our method compared to other approaches, with results sourced from their original papers. First, methods incorporating line features, such as PL-VINS, EPLF-VINS and MLINE-VINS, generally demonstrate higher accuracy than VINS-MONO. Second, EPLF-VINS and MLINE-VINS which utilize line tracking methods, tend to outperform PL-VINS. Additionally, methods incorporating structural constraints generally achieve better performance than conventional point-and-line-based approaches. By leveraging novel structural constraints in local and global optimization, our method demonstrates higher accuracy compared to UV-SLAM and Struct-VIO. Overall, the proposed method achieves the best performance, across most sequences, except for $MH04$. However, the performance of our system heavily depends on proper initialization. In particular, inaccuracies in the initial gyro bias occasionally degrade system performance. For the $MH02$, our method shows a 50.3% improvement in accuracy over Struct-VIO. These results highlight the effectiveness of our approach.

2) *KAIST-VIO Dataset Tests*: To evaluate the robustness of our system, we test our method on the KAIST-VIO dataset [31]. The dataset is collected by a UAV platform equipped with a monocular RGB camera(30 Hz) and IMU(100 Hz). It includes four different sports, each with three modes: normal, fast and rotation, which are challenging for VIO systems. We compare our method with VINS-MONO [5], EPLF-VINS [13],

TABLE III
TRANSLATION RMSE ATE WITHOUT LOOP CLOSURE OF KAIST-VIO DATASET (UNIT: M)

| Method | cir_f | cir_n | cir_r | inf_f | inf_n | inf_r | rot_f | rot_n | squ_f | squ_n | squ_r |
|------------------|--------------|--------------|--------------|--------------|--------------|--------------|--------------|--------------|--------------|--------------|--------------|
| VINS-MONO [5] | 0.126 | 0.234 | 0.257 | 0.080 | 0.055 | 0.360 | 0.337 | — | 0.061 | 0.077 | — |
| PL-VINS [7] | 0.119 | 0.122 | 0.305 | 0.063 | 0.057 | 0.415 | 0.527 | — | 0.062 | 0.145 | 0.232 |
| EPLF-VINS [13] | 0.144 | 0.069 | 0.437 | 0.234 | 0.129 | 0.461 | 0.206 | — | 0.094 | 0.097 | 0.308 |
| UV-SLAM [18] | 0.100 | 0.100 | 0.324 | 0.086 | 0.054 | 0.382 | 0.473 | — | 0.077 | 0.079 | — |
| MLINE-VINS(ours) | 0.095 | 0.051 | 0.118 | 0.130 | 0.051 | 0.306 | 0.143 | 0.212 | 0.087 | 0.066 | 0.206 |

PL-VINS [7] and UV-SLAM [18]. All other operations are the same as those used in the EuRoC dataset tests.

Table III shows the ATE RMSE results of all methods. Compared to other methods, our method demonstrates superior robustness. In particular, other methods tend to fail during rapid rotation scenarios due to difficulties in estimating relationships between frames. Our method operates reliably thanks to the local and global Manhattan constraints. It is important to note that point and line features can sometimes be unreliable in a rapidly changing scenarios, as triangulation may fail during quick camera rotations. With the aid of *MFs*, the UV-SLAM and MLINE-VINS can incorporate additional constraints in optimization. Besides, by leveraging the novel line tracking method and Manhattan constraints optimization, our method achieves higher accuracy.

B. Qualitative Evaluation

To better evaluate our method, we conduct several qualitative evaluation experiments.

1) *Evaluation of Line Segment Tracking*: We evaluate the number of line features tracked across consecutive frames by comparing our method with EPLF-VINS on the EuRoC dataset, as shown in Fig.10. By accounting for changes in line length during modeling, our method identifies more matching lines than EPLF-VINS.

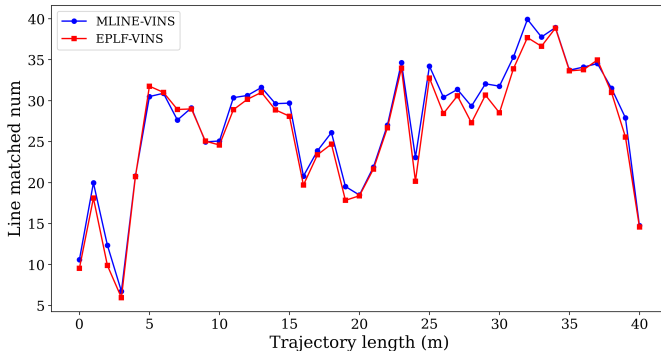


Fig. 10. Average number of line matches between MLINE-VINS and EPLF-VINS in EuRoC tests. The blue line represents the number of lines tracked by MLINE-VINS (ours), and the red line represents the number of lines tracked by EPLF-VINS.

2) *Evaluation of Drift in Challenging Environment*: To assess the drift of the proposed method, we compare the cumulative error across different methods using the KAIST-VIO dataset. Fig.11 presents the tracking trajectory and drift

errors for each method on the *cir_n* sequence. As shown, incorporating additional line features significantly reduces drift compared to only point-based methods, particularly during rotation. Compared to simple point and line features, structural regularity offers a more reliable means of constraining drift in both translation and rotation. By leveraging novel line feature tracking and Manhattan constraints, our method achieves the best performance with the least drift.

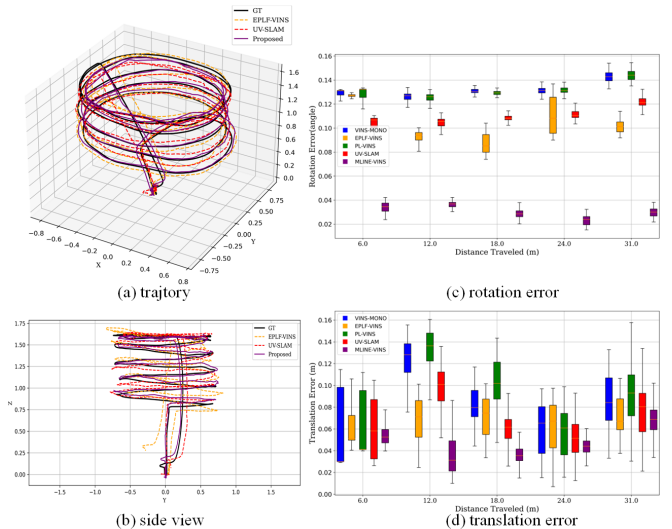


Fig. 11. Trajectory and relative pose error on the KAIST-VIO test. (a) and (b) show the trajectory of our method, EPLF-VINS and UV-SLAM. (c) and (d) show the average relative pose error for rotation and translation of each method.

3) *Evaluation of Vanishing Point Estimation*: We compare the runtime of different Manhattan estimation methods, including VPs estimation and structural lines classification, as shown in Fig.12. The 2-line method [17] requires the most time because it repeatedly executes RANSAC across all three directions. While MF Searching [25] is faster than the 2-line method, its performance is more sensitive to the number and distribution of lines. Benefiting from the proposed tracking-by-detection module for *Mfs* estimation, the proposed method achieves superior efficiency compared to the advanced approaches.

We also evaluate the performance of different *MF* estimation methods per frame, as shown in Fig.13. The MF Searching struggles to provide accurate *MF* estimations when line features are insufficient. The 2-line method fails under uneven line distribution. Besides, both the MF Searching and the 2-line method encounter issues with random and disordered

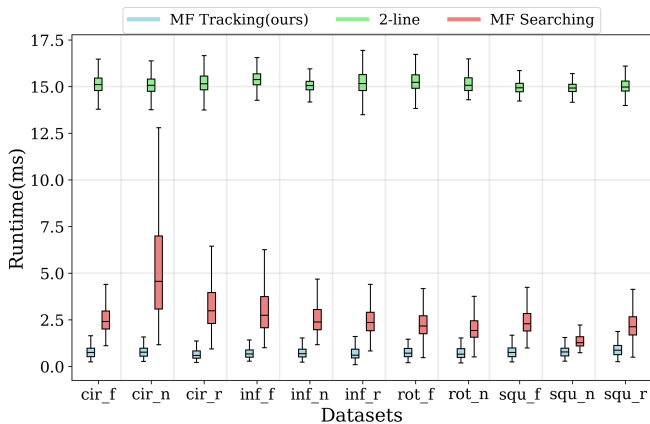


Fig. 12. Runtimes of *MF* estimation using MF Tracking (ours), 2-line and MF Searching in KAIST-VIO dataset

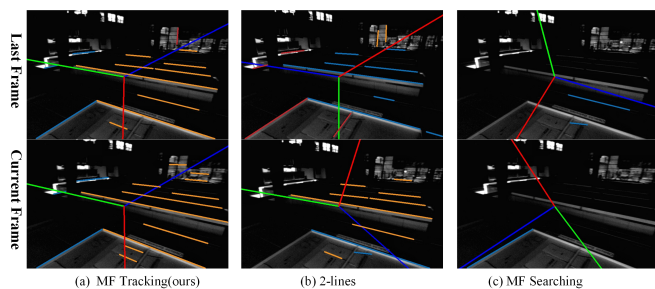


Fig. 13. *MFs* estimation in consecutive frames. (a), (b) and (c) show the results of *MFs* estimation using the Tracking-by-Detection Strategy (ours), the 2-line method and the MF Searching. The top image shows the last frame, and the bottom image shows the current frame.

Manhattan axes. In contrast, our method demonstrates stable and accurate performance across consecutive frames, making it suitable for real-world applications.

C. Real World Tests

In this section, we present real-world experiments to evaluate the performance of the proposed method in various indoor scenes. We use D435I camera and its internal IMU to collect RGB images and IMU messages for evaluation. RGB images are 640×480 recorded at 30 Hz and IMU messages are at 200 Hz. The camera and IMU are calibrated using Kalibr [32] and Imu_Utils [33]. In these experiments, all features including points and lines, are extracted directly from the original images. The datasets used are illustrated in Fig.14.

1) *Small Indoor Scene*: First, the proposed method is evaluated in a small indoor laboratory setting. As shown in Fig.14, the data is collected under two distinct conditions: slow rotation (referred to as *Weak-texture Easy*) and rapid rotation (referred to as *Weak-texture Hard*). We use motion capture equipment to obtain ground truth data and RMSE to evaluate performance.

For other methods, the default parameters are used in the experiments. The back-end of UV-SLAM does not perform well in real-world scenarios, resulting in failure across all

sequences. The RMSE results are shown in Table IV. MLINE-VINS achieves the best performance on both *Weak-texture Easy* and *Weak-texture Hard* datasets. On the *Weak-texture Hard* dataset, which includes pure rotation and fast movements, traditional line-matching methods occasionally fail.

TABLE IV
TRANSLATION RMSE ATE WITHOUT LOOP CLOSURE OF COLLECTED DATASET (UNIT: M)

| Method | VINS-MONO | PL-VINS | EPLF-VINS | MLINE-VINS(ours) |
|-------------------|-----------|---------|-----------|------------------|
| Weak-texture Easy | 0.316 | 0.218 | 0.357 | 0.216 |
| Weak-texture Hard | 0.365 | 0.528 | 0.248 | 0.227 |
| Average | 0.341 | 0.373 | 0.302 | 0.221 |

2) *Large Indoor Scene*: To further evaluate our method in real-world scenarios, we conducted experiments in a large indoor environment. In this setting, the camera traverses the first and second floors, eventually returning to the starting point. During this process, there are many challenging situations, including motion blur and weakly textured scenes as illustrated in Fig.14(c).

Unlike the small indoor scene, we evaluate the performance of each method based on the drift between the start and end points, which are at the same position. Since UV-SLAM cannot complete the entire trajectory, its results omitted. The results, shown in Fig.15, indicate that MLINE-VINS demonstrates superior performance in suppressing long-term accumulated errors. By incorporating Manhattan constraints into both local and global optimization, the proposed method achieves the best performance with minimal drift error.

D. Runtime Analysis

The computational performance of each module was evaluated on a per-frame basis, as shown in Table V. Our method and EPLF-VINS demonstrated superior efficiency in line feature detection and matching, primarily due to the implemented line tracking algorithm. Furthermore, the proposed tracking-by-detection module for *MFs* estimation proved to be more computationally efficient than the 2-lines method employed in UV-SLAM. Despite incorporating additional line features and Manhattan constraints, the Local VIO is not burdened significantly. Although the runtime of our method is slightly higher than that of VINS-MONO, it is still acceptable for real-time applications.

VI. CONCLUSION

In this paper, we introduce MLINE-VINS, a novel visual-inertial odometry system that integrates line features and Manhattan World constraints. To achieve real-time performance, we introduce a novel line feature tracking algorithm and tracking-by-detection module, which efficiently tracks variable-length lines and detects Manhattan frame across consecutive images. To simplify coordinate transformations, we align the VIO world frame with the Manhattan World framework. A pose-guided Manhattan frame verification mechanism

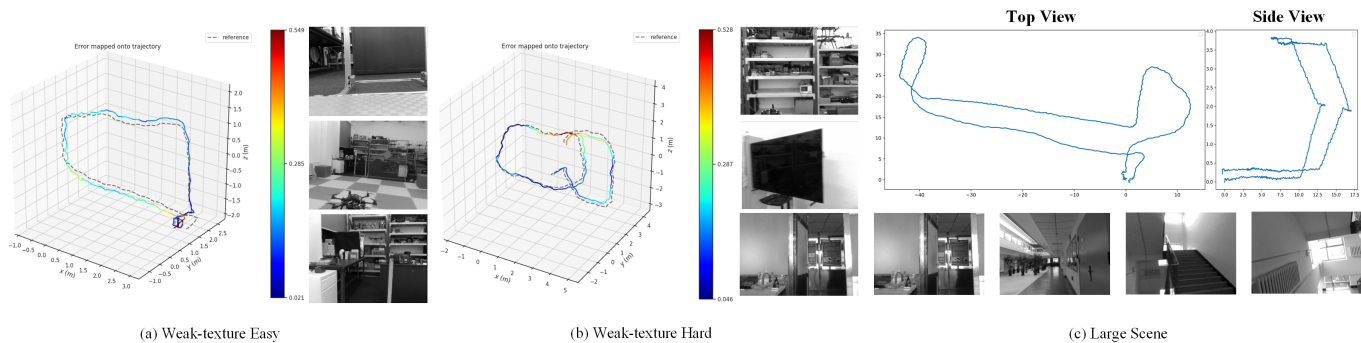


Fig. 14. Our collected data for evaluation VIO methods. For each sequence, we present the corresponding trajectory visualizations (left) and sample images (right). The datasets include (a) *Weak-texture Easy* and (b) *Weak-texture Hard* sequences captured in a small indoor environment equipped with motion capture systems for ground truth measurements and (c) *Large Scene* sequence containing long corridor scenes. These datasets cover various challenging scenarios, including motion blur, texture-deficient surfaces, and pure rotational movements.

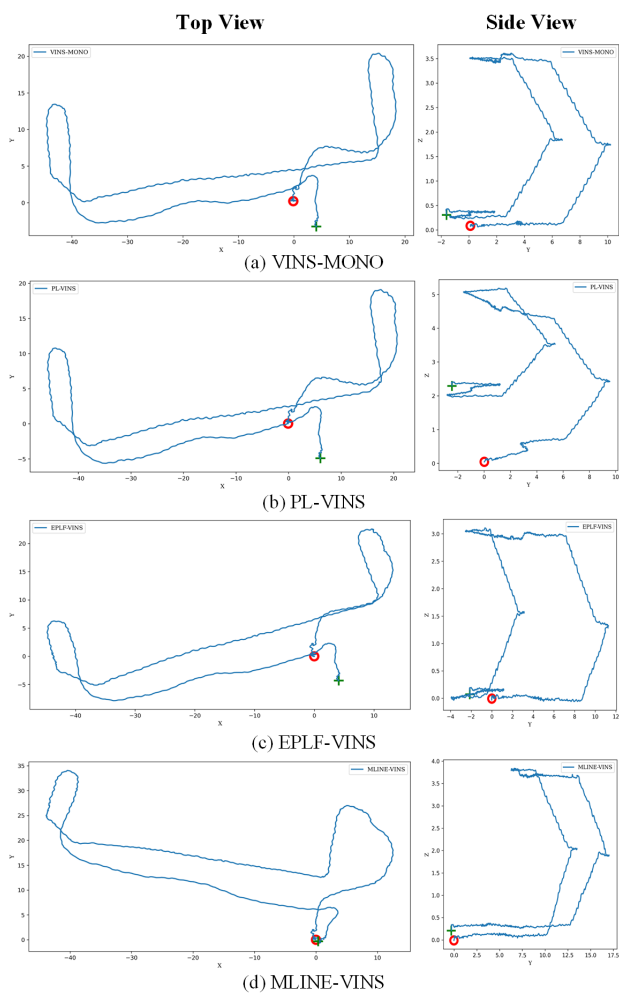


Fig. 15. Results of *Large Scene* test. The left image shows the top view of the trajectory, while the right image displays the side view. The red circle represents the starting point, and the green cross marks the endpoint.

is employed to ensure the reliability of the Manhattan frames. By incorporating structural lines and Manhattan frame constraints, we propose a novel back-end optimization framework that incorporates both local and global constraints to enhance the system's accuracy and robustness. Comprehensive eval-

TABLE V
RUNTIME OF EACH MODULE(MS)

| Thread | Module | VINS-MONO | PL-VINS | EPLF-VINS | UV-SLAM | MLINE-VINS |
|--------|--------------------------------|-----------|---------|-----------|---------|------------|
| 1 | Points Detection & Matching | 13.15 | 13.71 | 13.34 | 13.56 | 13.29 |
| 2 | Lines Detection & Matching | — | 33.03 | 14.37 | 22.09 | 14.80 |
| 3 | Manhattan Detection & Matching | — | — | — | 16.47 | 4.73 |
| 4 | Local VIO | 41.12 | 52.50 | 51.55 | 86.61 | 61.13 |

uations on benchmark and custom datasets demonstrate that MLINE-VINS achieves advanced performance in terms of both accuracy and robustness. In future work, we will focus on leveraging line features to further enhance the system's robustness and accuracy, particularly in challenging outdoor environments

REFERENCES

- [1] Z. Yang, Y. Li, J. Lin, Y. Sun, and J. Zhu, "wmps-slam: An online and accurate monocular visual-wmps slam system," *IEEE Transactions on Instrumentation and Measurement*, vol. 72, pp. 1–11, 2023.
- [2] S. Lin, J. Wang, M. Xu, H. Zhao, and Z. Chen, "Contour-slam: A robust object-level slam based on contour alignment," *IEEE Transactions on Instrumentation and Measurement*, vol. 72, pp. 1–12, 2023.
- [3] K. Sun, K. Mohta, B. Pfrommer, M. Watterson, S. Liu, Y. Mulgaonkar, C. J. Taylor, and V. Kumar, "Robust stereo visual inertial odometry for fast autonomous flight," *IEEE Robotics and Automation Letters*, vol. 3, no. 2, pp. 965–972, 2018.
- [4] S. Leutenegger, A. Forster, P. Furgale, P. Gohl, and S. Lynen, "Okvis: Open keyframe-based visual-inertial slam (ros version)," 2016.
- [5] T. Qin, P. Li, and S. Shen, "Vins-mono: A robust and versatile monocular visual-inertial state estimator," *IEEE Transactions on Robotics*, vol. 34, no. 4, pp. 1004–1020, 2018.
- [6] H. Si, H. Yu, K. Chen, and W. Yang, "Point-line visual-inertial odometry with optimized line feature processing," *IEEE Transactions on Instrumentation and Measurement*, vol. 73, pp. 1–13, 2024.
- [7] Q. Fu, J. Wang, H. Yu, I. Ali, F. Guo, Y. He, and H. Zhang, "Pl-vins: Real-time monocular visual-inertial slam with point and line features," *arXiv preprint arXiv:2009.07462*, 2020.
- [8] Y. He, J. Zhao, Y. Guo, W. He, and K. Yuan, "Pl-vio: Tightly-coupled monocular visual-inertial odometry using point and line features," *Sensors*, vol. 18, no. 4, p. 1159, 2018.
- [9] H. Jiang, R. Qian, L. Du, J. Pu, and J. Feng, "Ul-slam: A universal monocular line-based slam via unifying structural and non-structural constraints," *IEEE Transactions on Automation Science and Engineering*, pp. 1–18, 2024.

- [10] R. G. Von Gioi, J. Jakubowicz, J.-M. Morel, and G. Randall, "Lsd: A fast line segment detector with a false detection control," *IEEE transactions on pattern analysis and machine intelligence*, vol. 32, no. 4, pp. 722–732, 2008.
- [11] L. Zhang and R. Koch, "An efficient and robust line segment matching approach based on lbd descriptor and pairwise geometric consistency," *Journal of visual communication and image representation*, vol. 24, no. 7, pp. 794–805, 2013.
- [12] Q. Wang, Z. Yan, J. Wang, F. Xue, W. Ma, and H. Zha, "Line flow based simultaneous localization and mapping," *IEEE Transactions on Robotics*, vol. 37, no. 5, pp. 1416–1432, 2021.
- [13] L. Xu, H. Yin, T. Shi, D. Jiang, and B. Huang, "Eplf-vins: Real-time monocular visual-inertial slam with efficient point-line flow features," *IEEE Robotics and Automation Letters*, vol. 8, no. 2, pp. 752–759, 2023.
- [14] J. Coughlan and A. L. Yuille, "The manhattan world assumption: Regularities in scene statistics which enable bayesian inference," in *Advances in Neural Information Processing Systems*, T. Leen, T. Dietterich, and V. Tresp, Eds., vol. 13. MIT Press, 2000. [Online]. Available: https://proceedings.neurips.cc/paper_files/paper/2000/file/90e1357833654983612fb05e3ec9148c-Paper.pdf
- [15] H. Li, J. Yao, J.-C. Bazin, X. Lu, Y. Xing, and K. Liu, "A monocular slam system leveraging structural regularity in manhattan world," in *2018 IEEE International Conference on Robotics and Automation (ICRA)*. IEEE, 2018, pp. 2518–2525.
- [16] D. Zou, Y. Wu, L. Pei, H. Ling, and W. Yu, "Structvio: Visual-inertial odometry with structural regularity of man-made environments," *IEEE Transactions on Robotics*, vol. 35, no. 4, pp. 999–1013, 2019.
- [17] X. Lu, J. Yaoy, H. Li, Y. Liu, and X. Zhang, "2-line exhaustive searching for real-time vanishing point estimation in manhattan world," pp. 345–353, 2017.
- [18] H. Lim, J. Jeon, and H. Myung, "Uv-slam: Unconstrained line-based slam using vanishing points for structural mapping," *IEEE Robotics and Automation Letters*, vol. 7, no. 2, pp. 1518–1525, 2022.
- [19] C. Schmid and A. Zisserman, "Automatic line matching across views," in *Proceedings of IEEE Computer Society Conference on Computer Vision and Pattern Recognition*. IEEE, 1997, pp. 666–671.
- [20] O. Chum, J. Matas, and J. Kittler, "Locally optimized ransac," in *Pattern Recognition: 25th DAGM Symposium, Magdeburg, Germany, September 10-12, 2003. Proceedings 25*. Springer, 2003, pp. 236–243.
- [21] Z. Wang, F. Wu, and Z. Hu, "Msls: A robust descriptor for line matching," *Pattern Recognition*, vol. 42, no. 5, pp. 941–953, 2009.
- [22] D. Yan, H. Jiang, T. Li, and C. Shi, "Efficient vanishing point estimation for accurate camera rotation estimation in indoor environments," *IEEE Robotics and Automation Letters*, 2023.
- [23] H. Wei, F. Tang, Z. Xu, C. Zhang, and Y. Wu, "A point-line vio system with novel feature hybrids and with novel line predicting-matching," *IEEE Robotics and Automation Letters*, vol. 6, no. 4, pp. 8681–8688, 2021.
- [24] S. Baker and I. Matthews, "Lucas-kanade 20 years on: A unifying framework," *International journal of computer vision*, vol. 56, pp. 221–255, 2004.
- [25] H. Li, J. Zhao, J.-C. Bazin, and Y.-H. Liu, "Quasi-globally optimal and near/true real-time vanishing point estimation in manhattan world," *IEEE Transactions on Pattern Analysis and Machine Intelligence*, vol. 44, no. 3, pp. 1503–1518, 2020.
- [26] J. Shi and Tomasi, "Good features to track," in *1994 Proceedings of IEEE Conference on Computer Vision and Pattern Recognition*, 1994, pp. 593–600.
- [27] J. K. Suhr, "Kanade-lucas-tomasi (klt) feature tracker," *Computer Vision (EEE6503)*, pp. 9–18, 2009.
- [28] P. J. Huber, "Robust estimation of a location parameter," in *Breakthroughs in statistics: Methodology and distribution*. Springer, 1992, pp. 492–518.
- [29] S. Agarwal, K. Mierle *et al.*, "Ceres solver: Tutorial & reference," *Google Inc*, vol. 2, no. 72, p. 8, 2012.
- [30] M. Burri, J. Nikolic, P. Gohl, T. Schneider, J. Rehder, S. Omari, M. W. Achtelik, and R. Siegwart, "The euroc micro aerial vehicle datasets," *The International Journal of Robotics Research*, vol. 35, no. 10, pp. 1157–1163, 2016.
- [31] J. Jeon, S. Jung, E. Lee, D. Choi, and H. Myung, "Run your visual-inertial odometry on nvidia jetson: Benchmark tests on a micro aerial vehicle," *IEEE Robotics and Automation Letters*, vol. 6, no. 3, pp. 5332–5339, 2021.
- [32] P. Furgale, J. Rehder, and R. Siegwart, "Unified temporal and spatial calibration for multi-sensor systems," in *2013 IEEE/RSJ International Conference on Intelligent Robots and Systems*. IEEE, 2013, pp. 1280–1286.
- [33] O. J. Woodman, "An introduction to inertial navigation," University of Cambridge, Computer Laboratory, Tech. Rep., 2007.